Reversible O–O Bond Scission and O_2 evolution at MOF-supported Tetramanganese Clusters

Xin He[1], Tzuhsiung Yang[2], Andrei Iliescu,[1] Maxx Q. Arguilla[1], Tianyang Chen[1], Heather J. Kulik[2] & Mircea Dincă[1*]

[1]Department of Chemistry, Massachusetts Institute of Technology, 77 Massachusetts Avenue, Cambridge, Massachusetts 02139, USA. [2]Department of Chemical Engineering, Massachusetts Institute of Technology, 77 Massachusetts Avenue, Cambridge, Massachusetts 02139, USA. *e-mail: mdinca@mit.edu

The scission of the O–O bond in O_2 and the formation of O–O bonds during the evolution of O_2 in photosynthesis are the engines of aerobic life as we know it.[1,2] Likewise, the reduction of O_2 and its reverse, the oxidation of reduced oxygen species to form O_2, are indispensable components of emerging renewable technologies for energy storage and conversion.[3,4] Storing and unleashing the energy contained within the O_2 molecule requires control over the formation or scission of the four-electron double bond between two oxygen atoms. Nature performs these demanding multi-electron transformations by distributing the redox burden among multiple metal ions: evolution created metalloenzymes with polynuclear clusters wherein metal ions act in concert to deliver or accept multiple electrons. Most relevant in this sense are the tetramanganese-calcium (Mn_4CaO_5) cluster in the oxygen-evolving complex of photosystem II,[1] responsible for O_2 formation, and the tricopper clusters in multi-copper oxidases, which mediate O_2 reduction.[2] The critical step in both O_2 reduction and O_2 evolution is the interconversion between multinuclear metal-oxo species, where the O atoms carry formal –2 charges, and O–O bonded species where the oxygen atoms are more oxidized.[5,6] Attempts to mimic the natural systems with synthetic analogs have led to a number of elegant molecular clusters that shed light on the electron transfer events and stepwise mechanism of O–O bond cleavage and formation.[7-19] To our knowledge, however, the interconversion between molecular O_2 and metal-oxo species in either synthetic or enzymatic discrete systems has not been documented. Here, we report that a tetramangenese cluster formed by self-assembly within a metal–organic framework (MOF) spontaneously cleaves the oxygen-oxygen double bond and reduces O_2 by four electrons at room temperature. The ensuing tetranuclear manganese-oxo cluster engages in weak C–H bond activation and, more importantly, is competent for O–O bond formation and O_2 evolution at elevated temperature, enabled by the head-to-head orientation of two fully reduced oxo atoms that bridge neighboring Mn pairs. This study demonstrates the viability of four-electron interconversion between molecular O_2 and metal-oxo species and highlights the importance of site-isolation for achieving multi-electron chemistry at polynuclear metal clusters.

Multinuclear Mn clusters are particularly attractive as potential open sites for realizing multi-electron O_2 chemistry. In their reduced state, the manganese atoms provide multiple reducing equivalents and binding sites for oxygen reduction, reminiscent of multi-copper oxidases (MCOs) and cytochrome C oxidase (CcO),[2,20] which bind and reduce O_2 in an electron rich "pocket" featuring multiple redox active open sites. Similarly, in the oxygen-evolving complex (OEC) of photosystem II, the Mn_4Ca cluster provides not just multiple oxidizing equivalents, but also four independent O-binding sites. Synthesizing molecular mimics capable of four-electron redox chemistry, which also provide multiple inward-oriented open metal sites for oxygen binding, as would be required for O–O coupling reactivity, has been difficult.[13,14,21,22] Furthermore, molecular mimics operating in solution are challenged by deleterious H-atom abstraction reactions that compete with bimolecular coupling of terminal or bridging oxo species that would give rise to O_2. We sought to circumvent these issues by exploiting the site-isolation and potential for multi-electron chemistry of MOFs with multi-nuclear secondary-building units (SBUs).[23] The porous nature of MOFs enables solid-gas reactivity and flow chemistry without interference from solvent molecules, while the inherent site isolation of SBUs prevents intermolecular decay pathways. Functionally, this behavior is not unlike that of metalloenzymes, where the protein complex allows access of only specific molecules to the active site, and evidently also prevents active sites from reacting with each other. One material that provides many of the features we identified as necessary for multi-electron O_2 reactivity is $Mn_3[(Mn_4Cl)_3BTT_8]_2$ (MnMnBTT, **1**, BTT = 1,3,5-benzenetristetrazolate).[24] This MOF is made from BTT-bridged $[Mn_4Cl]^{7+}$ SBUs wherein Mn^{2+} ions sit in a square-planar arrangement and are bridged by a weakly-coordinated chloride (Cl···Mn distance = 2.6725(10) Å) **(**Fig. 1b–d). We hypothesized that removal of the central chloride anion would generate four inward-oriented open metal sites that would be primed for interacting with small molecules. Owing to their robust redox chemistry, the Mn atoms could thus engage particularly well with redox-active small molecules such as O_2 (Fig. 1a).

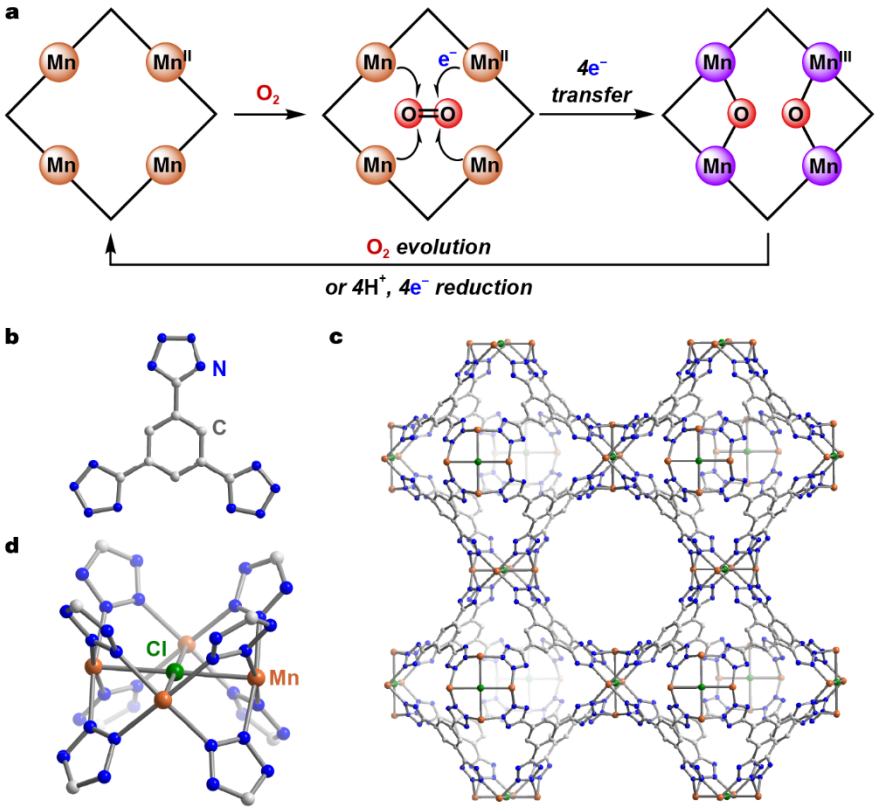

Fig. 1 | O_2 fixation and evolution at a site-isolated tetramanganese cluster with open metal sites. a, Schematic representation of oxygen reduction and evolution through the intermediacy of bridging oxo species. **b**, Structure of the BTT^{3-} ligand. **c**, Secondary building unit (SBU) of MnMnBTT formed by a $[Mn_4Cl]^{7+}$ core and eight bridging tetrazolate rings. **d**, Crystal structure of MnMnBTT. Hydrogen atoms, solvent molecules and charge-balancing extraframework Mn atoms are omitted for clarity.

Soaking as-synthesized crystals of **1** in methanol for two weeks eliminates $MnCl_2$ equivalents according to the equation $Mn_3[(Mn_4Cl)_3BTT_8]_2 \rightarrow 2(Mn_4)_3BTT_8 + 3MnCl_2$. This generates a material wherein 13% of all SBUs are chloride-deficient. Activation by heating this material at 120 °C and dynamic vacuum removes most solvent molecules and generates a material with Mn_4 clusters that are free of both solvent and chloride (MnMnBTT-v, **2**) (Fig. 2a). The amount of $MnCl_2$ "leached" out of **1** to produce **2** was confirmed by a combination of X-ray photoelectron spectroscopy (XPS), ion chromatography (IC), and inductively coupled plasma mass spectrometry (ICP-MS) (Fig. 2b, Supplementary Table 1, and Supplementary Figs. 1–4). Formation of AgCl precipitate upon addition of $AgBF_4$ to the methanolic filtrate collected after $MnCl_2$ elimination confirmed the leaching of chloride anions from MOF SBUs (Supplementary Fig. 5). Compound **2** retains crystallinity and porosity after the soaking process, as confirmed by powder X-ray diffraction (PXRD, Supplementary Fig. 6) and an N_2 adsorption isotherm, which gave an apparent BET surface area of

2301 m^2/g (Supplementary Fig. 7), slightly larger than the parent material.[24]

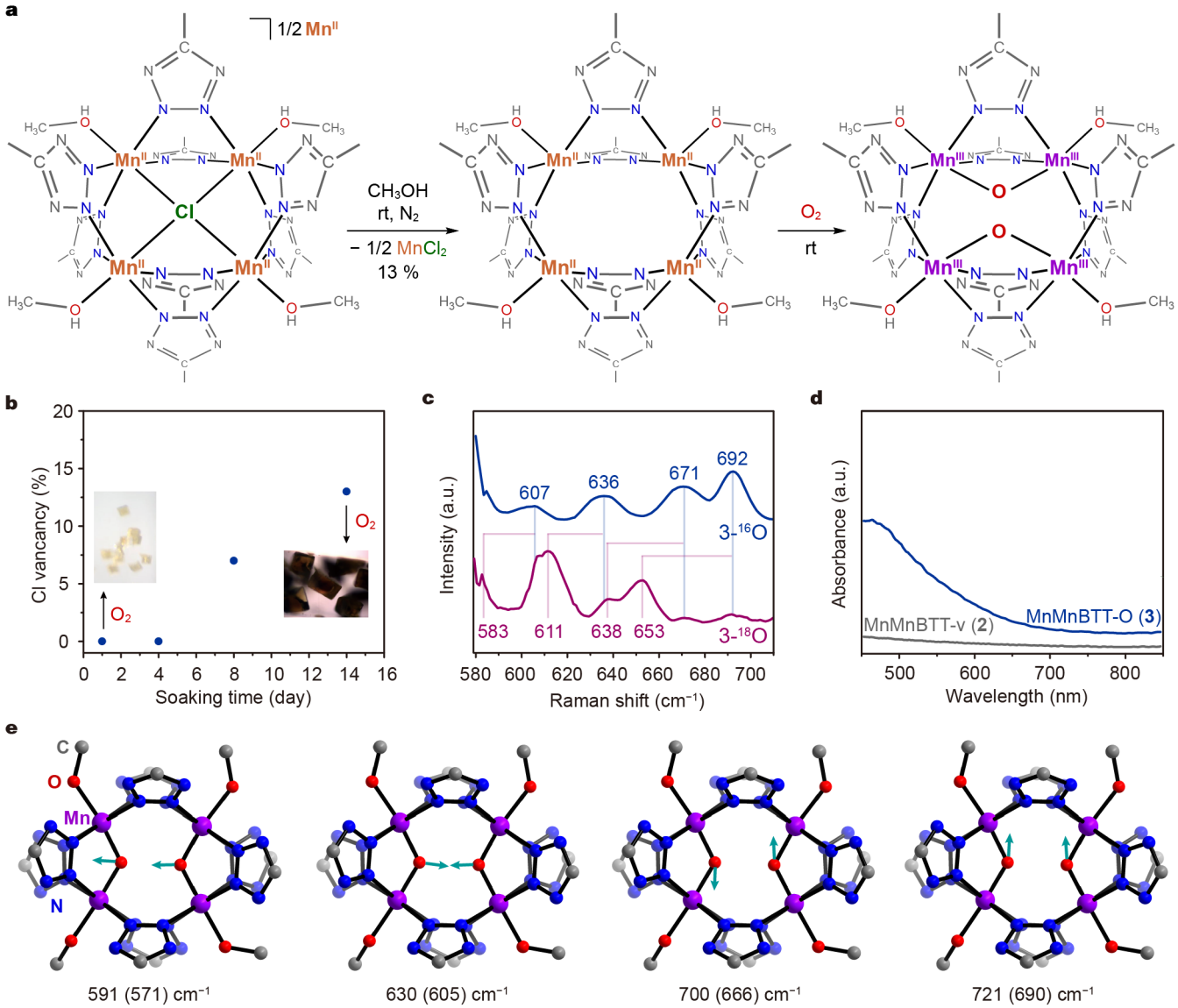

Fig. 2 | Generation of tetramanganese sites and oxygen reduction reactivity. a, Generation of tetramanganese open site and its O_2 reduction reactivity. **b**, Average chloride vacancy in each SBU determined by XPS, as a function of methanol soaking time. Insets show the color of activated, O_2-exposed samples that were soaked in methanol for 1 day and 14 days, respectively. **c**, Raman spectra of **3-^{16}O** and **3-^{18}O**. **d**, Electronic absorption spectra of **2** and **3**. **e**, Simulated vibrational modes and corresponding frequencies for the [Mn_4(***μ*-O**)$_2$(tetrazole)$_8$(CH_3OH)$_4$] unit. Vibrational frequencies for ^{18}O models are shown in parentheses.

Treatment of **2** with dry O_2 under strictly moisture-free conditions at room temperature yields dark-brown crystals of MnMnBTT-O (**3**, Supplementary Fig. 8). Compound **3** exhibits broad absorption in the visible and near infrared range (λ_{max} = 464 nm), contrasting with **2**, which shows negligible absorption in these regions, as would be expected for Mn^{II} compounds. The strong electronic absorption in **3** is clearly

indicative of oxidation at the Mn sites (Fig. 2c). Importantly, crystals of **1** that lack chloride vacancies do not show any visible changes upon exposure to O_2, suggesting that only those Mn_4 clusters that have internal open coordination sites produced by chloride elimination are responsible for O_2 reactivity (Fig. 2a). A Raman spectrum of **3** shows four bands at 607, 636, 671 and 692 cm^{-1}. These bands are significantly lower in energy than the reported ν_{O-O} frequencies for Mn(III)-peroxo (819–885 cm^{-1}) and Mn(III)-superoxo (1124 cm^{-1}) compounds, ruling out the formation of peroxo or superoxo species in **3**.[25-27] More in line with the vibrational features in **3** are bis(μ-oxo) dimanganese units,[28] which display a multitude of peaks between 600 cm^{-1} and 700 cm^{-1}, pointing to full O–O bond cleavage and the formation of μ-oxo in **3**. ^{18}O-labeling studies revealed that the low-frequency Raman bands are all isotopically sensitive: upon treatment of **2** with $^{36}O_2$, the four Raman bands all shift, to 583, 611, 638 and 653 cm^{-1}, respectively (Fig. 2d and Supplementary Fig. 13). Corroborating the formation of bis(μ-oxo) dimanganese units in the vacant Mn_4 clusters are density functional theory (DFT) calculations. Structural optimization and analysis of a truncated model cluster built from four Mn ions, two oxygen atoms, eight tetrazole rings, and four methanol molecules coordinated *exo* to each Mn ion (Fig. 2e) indicates all manganese ions are in the +III formal oxidation state, as would be expected for a cooperative four-electron reduction of O_2 (Fig. 2e and Supplementary Fig. 9). Computed vibrational frequency analysis gives four scaled vibrational modes at 591, 630, 700, and 721 cm^{-1}, which shift to 571, 605, 666 and 690 cm^{-1} for the ^{18}O model, in excellent agreement with the experimental Raman bands assigned to the dimanganese μ-oxo species (Fig. 2e and Supplementary Fig. 14). Notably, computational models involving incomplete O–O bond cleavage, that is, formation of dioxygen, superoxo, or peroxo species, gave vibrational frequencies of 1455 cm^{-1}, 1243 cm^{-1}, and 883 cm^{-1}, respectively, for the O–O stretch (Supplementary Figs. 15–19), which are not observed in **3**.

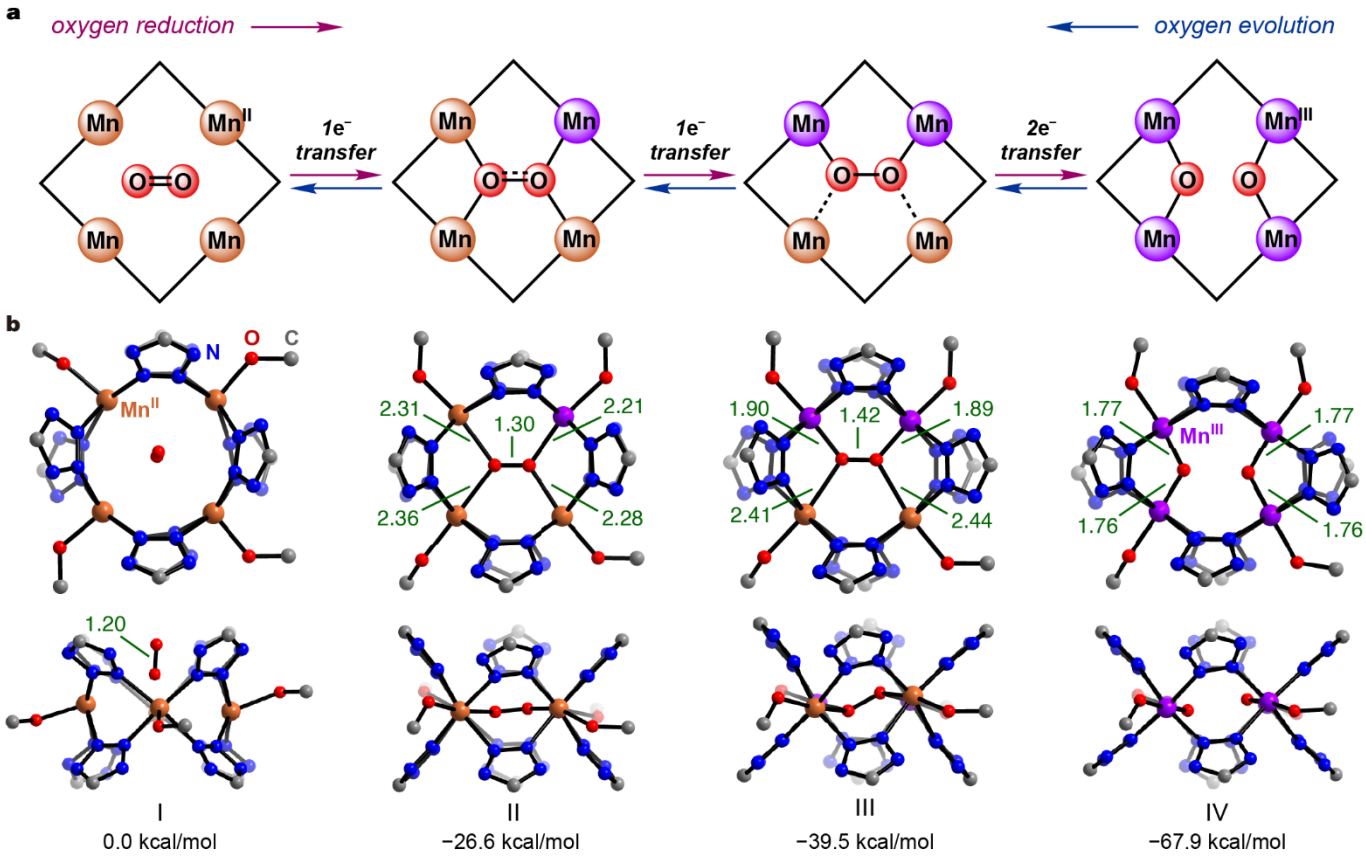

Fig. 3 | Calculated reaction pathway for O_2 reduction and evolution at a tetramanganese site and free energies of reaction intermediates. a, Electron transfer sequence along the oxygen reduction (from left to right) and evolution (from right to left). **b**, Optimized structures shown normal and parallel to the plane formed by the four Mn ions in a Mn_4 cluster, with the associated free energy for: (I) native all-Mn^{II} cluster with O_2; (II) superoxo intermediate; (III) peroxo intermediate; (IV) all-Mn^{III} di-μ_2-oxo cluster. Hydrogen atoms are omitted. All distances are reported in Å.

Computational analysis provided a reasonable reaction pathway and intermediates during the scission of the O=O bond (Fig. 3). The first one-electron reduction of O_2 by the Mn_4 cluster gives a μ_2-η^2,η^2 superoxo intermediate II wherein one Mn^{II} is oxidized to Mn^{III} and the O–O bond is elongated by 0.1 Å to 1.30 Å, slightly longer than that of a reported monomeric end-on Mn^{III}-superoxo (1.249(4) Å)[26]. The second $1e^-$ transfer from an adjacent Mn^{II} to superoxide has a barrier of 1.2 kcal/mol and affords a trans-μ-1,2-peroxo intermediate III bearing a di-Mn^{III} unit (Supplementary Table 3 and Supplementary Fig. 20). In intermediate III, the Mn^{III}–O bonds are approximately 0.5 Å shorter than the other two Mn^{II}–O bonds. The Mn^{II} can therefore be thought of as Lewis acids that weakly coordinate the peroxide thus activating it for further electron transfer. The O–O bond in III is further elongated to 1.42 Å, and is comparable to those found in

binuclear Mn^{III}-peroxo species, 1.452(5) Å,[27] and mononuclear side-on Mn^{IV}-peroxo species, 1.415(2) Å.[29] Even though the final two-electron reduction of III to IV has a calculated barrier of 16.0 kcal/mol, it is exergonic by 28.4 kcal/mol and leads to complete cleavage of the O–O bond, with formation of the all-Mn^{III} [$Mn_4(\mu\text{-}O)_2$] core (species IV in Fig. 3) that is experimentally found in **3**. The tetramanganese core in IV deviates significantly from the original ~3.8 Å × 3.8 Å square shape to form a rectangle with approximate sides of 4.0 Å × 3.1 Å, wherein the O···O distance between the two μ-oxo units is 2.42 Å.

Functionally, the reduction of O_2 by **2** resembles O_2 reduction in MCOs and cytochrome C oxidase (CcO), where multiple Cu and/or Fe atoms reduce O_2 catalytically. To test whether **2** can also turn over and engage with O_2 catalytically, we treated **3** with cyclohexadiene, a H-atom donor here used as a sacrificial reductant, under an atmosphere of O_2. Under these conditions, **2** engages in 43.1 turnovers, measured as molecules of benzene produced per vacant Mn_4 cluster (table S2). Cyclohexadiene acts as the source of both reducing equivalents and protons in this reaction.

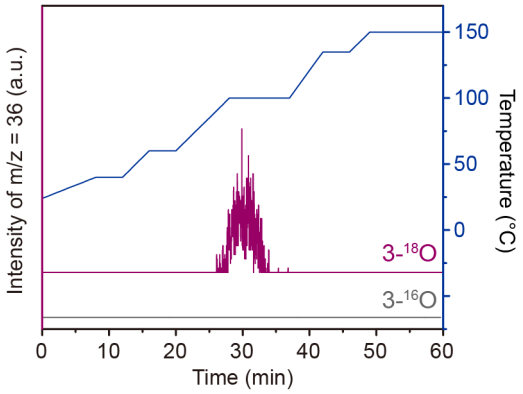

Fig. 4 | O_2 evolution from 3-^{18}O. Oxygen evolution reactions were conducted in a continuous, tubular flow reactor under helium flow. The intensity of m/z = 36 of the outlet gas was monitored using mass spectrometry.

In **3**, O_2 is reduced by four electrons at the Mn_4 cluster to give $[Mn^{III}_4(\mu\text{-}O)_2(\text{tetrazole})_8(CH_3OH)_4]$ units, as determined based on spectroscopic characterizations and density-functional theory (DFT) calculations (Fig. 2, *vide supra*). Previous reports of multielectron activation of O_2 typically involve trinuclear clusters;[13,14] our strategy here represents an alternative involving tetranuclear clusters that in this sense more closely mimics the oxygen evolving complex (OEC) of Photosystem II. Given the proximity and orientation of the two oxo groups within oxidized clusters in **3**, we envisioned a scenario where these groups could indeed couple to reversibly form an O–O bond and potentially even release O_2. To probe this scenario, we monitored O_2 generation using real-time in-line mass spectrometry (MS), following counts for species with a mass-to-charge ratio (m/z) of 32, for $^{32}O_2$. However, m/z = 32 also corresponds to methanol, traces of which are released from the MOF at temperatures exceeding 65 °C, and which interferes with the $^{32}O_2$ signal. Instead, we used $^{36}O_2$ to produce and isolate ^{18}O-labeled **3-^{18}O**. The labeled MOF was then evacuated and purged with He to remove any potential trace of left-over $^{36}O_2$. Gradually heating **3-^{18}O** and monitoring the m/z = 36 MS signal produces a clear peak around 100 °C (Fig. 4), which can only be assigned to $^{36}O_2$. In a control experiment, heating of **3** up to 150 °C under a flow of He gives no detectable signal for m/z = 36. PXRD confirmed that the framework remains crystalline after O_2 evolution. Considering the rigid framework, intermolecular reaction pathways for O_2 formation can be ruled out. Likewise, O_2 formation by oxidation of solvent molecules is unlikely as none of the possible trace or guest solvent molecules are labeled with ^{18}O. Thus, we assign the observed m/z = 36 signal to O_2 produced by coupling two bridging oxo groups in tetramanganese clusters.

The computational analysis in Figure 3 illustrates the reaction pathway for O_2 evolution. We note that the main driving force for O_2 evolution, which is endergonic, is the generation of gaseous O_2 in an open system. Starting from the manganese-oxide cluster, the first step is O–O bond formation via the interaction of two metal–oxo units. This step is particularly difficult and rarely observed in molecular systems, not least because the oxos require radical character.[6] Here, the radical character of the bridging oxos is revealed by their reactivity towards H-atom abstraction (vide supra). Notably, radical coupling and nucleophilic attack mechanisms for O_2 formation traditionally involve Mn^{IV}-oxyl radical and/or Mn^{V}–oxo electrophiles.[11] In our system, we show that high-valent manganese is not required for O_2 evolution in a tetramanganese cluster. The calculated energy barrier for O–O bond formation, 44.4 kcal/mol, is relatively large and may explain why O_2 generation from this system requires elevated temperature. One important advantage of this MOF system is likely the favorable orientation of the two coupling oxo groups, which are fixed by the Mn_4 cluster

in an entropically-favored conformation with a relatively short O···O distance of 2.42 Å. The subsequent steps are significantly less thermodynamically demanding, with O_2 release expected to be spontaneous upon forming the O–O bond. The last step, O_2 release, is essentially the reverse of a chemisorptive O_2 binding and is driven by running O_2 evolution in an open system under He flow. To our knowledge, this represents the first example of a discrete artificial Mn system that evolves O_2.

The presence of four Mn atoms in the O_2-evolving cluster in **3** allows one-electron redox processes at each Mn atom and raises the question of whether reactivity could be observed in the presence of just three Mn atoms. To test the necessity of all four Mn atoms, we targeted an isostructural trimanganese-mononickel cluster supported by the same tris-tetrazolate ligand. We had previously shown that partially substituted clusters can be accessed by post-synthetic metal exchanges in the parent all-manganese MOF.[30,31] We focused on the Ni-exchanged clusters because the less oxophilic Ni^{2+} is unlikely to allow oxidation to Ni^{3+}, thereby potentially forcing one of the remaining Mn atoms to engage in multielectron chemistry. Furthermore, upon removal of central chloride ions from Mn_3Ni clusters, Ni would adopt a favorable square-planar geometry. Thus, colorless crystals of **1** were soaked in a concentrated methanolic solution of anhydrous $NiCl_2$ at 50 °C for 18 hours. The resulting green material, solvated **1-Ni**, remains crystalline and preserves the topology of the starting material, as confirmed by PXRD (Supplementary Fig. 22), and maintains porosity (Supplementary Fig. 23). The Ni, Mn, and Cl content of **1-Ni**, calculated by XPS (Supplementary Fig. 24), IC, and ICP-MS measurements, allowed unambiguous assignment of the formula of **1-Ni** as $Ni_3[(Mn_{2.6}Ni_{1.4}Cl)_3(BTT)_8]_2$ whereby an average of 1.4 Mn cations are replaced by Ni in each tetrametal cluster. This assignment assumes full exchange of more labile extraframework cations. Even though the formula represents an average that allows for a mixture of clusters with varying compositions Ni_xMn_{4-x} (x = 0 – 4), the presence of Mn_4 clusters is ruled out by subsequent reactivity studies (vide infra). As with **1**, $NiCl_2$ equivalents can be removed from **1-Ni** by soaking it in MeOH to generate the chloride-vacant material **2-Ni** as a green crystalline solid, in the solvated state (Supplementary Fig. 22). In **2-Ni**, 14% of its tetranuclear clusters are chloride-deficient, as confirmed by ICP-MS, IC, and XPS analyses (Supplementary Fig. 25). Green crystals of **2-Ni** can be desolvated under dynamic vacuum at 120 °C for 18 hours to yield a tan, crystalline solid that retains the same structure as **2-Ni** (Supplementary Fig. 22). Importantly, dosing O_2 onto this tan solid does not result in a color change and yields no changes to the Raman spectrum (Supplementary Fig. 26). Notably, no new bands are observed at 607, 636, 671 or 692 cm^{-1} which also confirms that no Mn_4 clusters are present in **2-Ni**. Thus, exchange of at least one Mn ion in tetranuclear Mn_4 clusters by a metal

with an inaccessible oxidation potential eliminates all reactivity with O_2.

Our work provides structural and functional precedent for the interconversion between O_2 and metal–oxos, and offers insight into the four-electron cleavage and formation of O–O double bonds. Cleavage and formation of O=O bonds typically require independent chemical systems or metalloenzyme cofactors, but is achieved here in a single Mn_4 cluster. The results thus highlight both the utility of multinuclear clusters in mitigating the redox burden for multielectron processes, and the advantage of placing such clusters inside MOFs, to lower the entropic penalty for coupling two oxo groups and favor the formation of the O–O bond, often the rate determining step in O_2 evolution mechanisms. We expect to be able to extend these design principles for creating solid-state materials relevant to O_2 management, and more generally, for enabling multielectron activation processes of other small molecules such as CO_2 and N_2.

References

1. Kern, J. et al. Structures of the intermediates of Kok's photosynthetic water oxidation clock. *Nature* **563**, 421-425 (2018).
2. Solomon, E. I., Augustine, A. J. & Yoon, J. O_2 reduction to H_2O by the multicopper oxidases. *Dalton Trans.*, 3921-3932 (2008).
3. Kanan, M. W. & Nocera, D. G. In situ formation of an oxygen-evolving catalyst in neutral water containing phosphate and Co^{2+}. *Science* **321**, 1072 (2008).
4. Pegis, M. L., Wise, C. F., Martin, D. J. & Mayer, J. M. Oxygen reduction by homogeneous molecular catalysts and electrocatalysts. *Chem. Rev.* **118**, 2340-2391 (2018).
5. Halfen, J. A. et al. Reversible cleavage and formation of the dioxygen O–O bond within a dicopper complex. *Science* **271**, 1397 (1996).
6. Betley, T. A. et al. A ligand field chemistry of oxygen generation by the oxygen-evolving complex and synthetic active sites. *Philosophical Transactions of the Royal Society B: Biological Sciences* **363**, 1293-1303 (2008).
7. Blakemore, J. D., Crabtree, R. H. & Brudvig, G. W. Molecular catalysts for water oxidation. *Chem. Rev.* **115**, 12974-13005 (2015).
8. Elwell, C. E. et al. Copper–oxygen complexes revisited: Structures, spectroscopy, and reactivity. *Chem. Rev.* **117**, 2059-2107 (2017).
9. Adam, S. M. et al. Synthetic Fe/Cu complexes: Toward understanding heme-copper oxidase structure and function. *Chem. Rev.* **118**, 10840-11022 (2018).
10. Jasniewski, A. J. & Que, L. Dioxygen activation by nonheme diiron enzymes: Diverse dioxygen adducts, high-valent intermediates, and related model complexes. *Chem. Rev.* **118**, 2554-2592 (2018).
11. Zhang, B. & Sun, L. Artificial photosynthesis: Opportunities and challenges of molecular catalysts. *Chem. Soc. Rev.* **48**, 2216-2264 (2019).
12. Cole, A. P., Root, D. E., Mukherjee, P., Solomon, E. I. & Stack, T. D. P. A trinuclear intermediate in the copper-mediated reduction of O_2: Four electrons from three coppers. *Science* **273**, 1848 (1996).
13. Lionetti, D., Day, M. W. & Agapie, T. Metal-templated ligand architectures for trinuclear chemistry: Tricopper complexes and their O_2 reactivity. *Chem. Sci.* **4**, 785-790 (2013).
14. Cook, B. J., Di Francesco, G. N., Kieber-Emmons, M. T. & Murray, L. J. A tricopper(I) complex competent for O atom transfer, C–H bond activation, and multiple O_2 activation steps. *Inorg. Chem.* **57**, 11361-11368 (2018).
15. Kanady, J. S., Tsui, E. Y., Day, M. W. & Agapie, T. A synthetic model of the Mn_3Ca subsite of the oxygen-evolving complex in photosystem II. *Science* **333**, 733 (2011).
16. Mukherjee, S. et al. Synthetic model of the asymmetric $[Mn_3CaO_4]$ cubane core of the oxygen-evolving complex of photosystem II. *Proceedings of the National Academy of Sciences* **109**, 2257 (2012).
17. Zhang, C. et al. A synthetic Mn_4Ca-cluster mimicking the oxygen-evolving center of photosynthesis. *Science* **348**, 690 (2015).
18. Maayan, G., Gluz, N. & Christou, G. A bioinspired soluble manganese cluster as a water oxidation electrocatalyst with low overpotential. *Nat. Catal.* **1**, 48-54 (2017).
19. Dismukes, G. C. et al. Development of bioinspired Mn_4O_4−cubane water oxidation catalysts: Lessons from photosynthesis. *Acc. Chem. Res.* **42**, 1935-1943 (2009).
20. Collman, J. P. et al. A cytochrome C oxidase model catalyzes oxygen to water reduction under rate-limiting electron flux. *Science* **315**, 1565 (2007).

21. Powers, T. M. & Betley, T. A. Testing the polynuclear hypothesis: Multielectron reduction of small molecules by triiron reaction sites. *J. Am. Chem. Soc.* **135**, 12289-12296 (2013).
22. DeRosha, D. E. et al. Planar three-coordinate iron sulfide in a synthetic [4Fe-3S] cluster with biomimetic reactivity. *Nat. Chem.* **11**, 1019-1025 (2019).
23. Yaghi, O. M., Kalmutzki, M. J. & Diercks, C. S. *Introduction to reticular chemistry: Metal-organic frameworks and covalent organic frameworks*. (Wiley-VCH, 2019).
24. Dincă, M. et al. Hydrogen storage in a microporous metal-organic framework with exposed Mn^{2+} coordination sites. *J. Am. Chem. Soc.* **128**, 16876-16883 (2006).
25. Shook, R. L. et al. A monomeric Mn^{III}−peroxo complex derived directly from dioxygen. *J. Am. Chem. Soc.* **130**, 8888-8889 (2008).
26. Liu, L.-L. et al. A Mn(III)–superoxo complex of a zwitterionic calix[4]arene with an unprecedented linear end-on Mn(III)–O_2 arrangement and good catalytic performance for alkene epoxidation. *Chem. Commun.* **47**, 11146-11148 (2011).
27. Coggins, M. K. et al. Characterization of metastable intermediates formed in the reaction between a Mn(II) complex and dioxygen, including a crystallographic structure of a binuclear Mn(III)–peroxo species. *J. Am. Chem. Soc.* **135**, 5631-5640 (2013).
28. Limburg, J. et al. Characterization of the O_2-evolving reaction catalyzed by $[(terpy)(H_2O)Mn^{III}(O)_2Mn^{IV}(OH_2)(terpy)](NO_3)_3$ (terpy = 2,2':6,2"-terpyridine). *J. Am. Chem. Soc.* **123**, 423-430 (2001).
29. Hong, S. et al. Crystallographic and spectroscopic characterization and reactivities of a mononuclear non-haem iron(III)-superoxo complex. *Nat. Commun.* **5**, 5440 (2014).
30. Brozek, C. K., Cozzolino, A. F., Teat, S. J., Chen, Y.-S. & Dincă, M. Quantification of site-specific cation exchange in metal–organic frameworks using multi-wavelength anomalous X-ray dispersion. *Chem. Mater.* **25**, 2998-3002 (2013).
31. Dincă, M. & Long, J. R. High-enthalpy hydrogen adsorption in cation-exchanged variants of the microporous metal−organic framework $Mn_3[(Mn_4Cl)_3(BTT)_8(CH_3OH)_{10}]_2$. *J. Am. Chem. Soc.* **129**, 11172-11176 (2007).

Acknowledgements Work in the Dincă lab (X.H., A.I., T.C., M.D.) was supported by the National Science Foundation (DMR-2105495). Computational work was supported by the Inorganometallic Catalyst Design Center, an EFRC funded by the DOE, Office of Basic Energy Sciences (DE-SC0012702) to T.Y. and H.J.K. This work was carried out in part using computational resources from the Extreme Science and Engineering Discovery Environment (XSEDE), which is supported by National Science Foundation grant number ACI-1548562. We thank C. Sun for assistance with mass spectrometry, J. Oppenheim for assistance with gas adsorption measurements, and A. Nandy for assistance with TDDFT figures.

Author contributions X.H., A.I. and M.D. formulated the project. X.H. and A.I. conducted the synthesis of the materials, standard characterizations, and the reactivity study. T.Y. and H.J.K. carried out the DFT calculations. T.Y., X.H., and H.J.K. analyzed the DFT calculations. M.Q.A. and A.I. carried out the Raman spectroscopy and the hyperspectral imaging measurements. T.C. and A.I. carried out the X-ray photoelectron spectroscopy measurements. X.H., A.I. and M.D. interpreted the results and wrote the manuscript with input from all authors.

Competing interests The authors declare no competing interests.

Correspondence and requests for materials should be addressed to M.D.